

# Perspective on the muon-spin rotation/relaxation under pressure

Rustem Khasanov<sup>1</sup>

Laboratory for Muon Spin Spectroscopy, Paul Scherrer Institut, CH-5232 Villigen PSI, Switzerland

(\*Electronic mail: rustem.khasanov@psi.ch)

Pressure, together with temperature, electric and magnetic fields, alters the system and allows to investigate the fundamental properties of the matter. Under applied pressure the interatomic distances shrink, which modify interactions between atoms and may lead to appearance of a new (sometime exotic) physical properties as, *e.g.*, pressure induced phase transition(s); quantum critical points(s), new structural, magnetic and/or superconducting states; changes of the temperature evolution and the symmetry of the order parameter(s) *etc.*

The muon-spin rotation/relaxation ( $\mu$ SR) appears to be a commonly used powerful technique allowing to study the magnetic and superconducting responses of various materials under extreme conditions. At present,  $\mu$ SR experiments might be performed under the high magnetic field up to  $\sim 9$  T, temperatures down to  $\simeq 10 - 15$  mK and hydrostatic pressure up to  $\sim 2.8$  GPa. In the following Perspective paper the requirements to the  $\mu$ SR under pressure experiments, the existing high-pressure muon facility at the Paul Scherrer Institute (Switzerland), and selected experimental results obtained by using the  $\mu$ SR under pressure technique are discussed.

Keywords: muon-spin rotation/relaxation, pressure, magnetism, superconductivity

## I. INTRODUCTION

Muon-spin rotation/relaxation ( $\mu$ SR) experiments, provide information at an atomic level on the chemical and physical properties of the matter. Compared to some other microscopic techniques,  $\mu$ SR experiments are easy to conduct and rather straightforward to perform. Indeed, in  $\mu$ SR studies:

- a relatively complicated sample environment can be used as illustrated, *e.g.*, by the large number of measurements performed down to 10 mK in temperature, up to 9 T in magnetic field, up to 2.8 GPa under the pressure *etc.*;
- collecting of a single measurement point requires, in most cases, not more than one hour. In other words, in a reasonable amount of time it is possible to obtain the  $\mu$ SR response of the sample studied and to follow evolutions of its properties as a function of temperature, magnetic field, pressure *etc.*;
- the sample may stay in a different aggregate state, as, *e.g.*, gas, liquid or solid;
- the sample does not need to contain any specific nuclei as is required, *e.g.*, in NMR and NQR, experiments.

The high pressure research becomes one of the most significant areas in  $\mu$ SR studies as it allows fine tuning of different phases of the matter, as well as to follow their strong interaction/interplay. The importance of  $\mu$ SR under pressure studies led to fast development of the dedicated muon instrumentation.<sup>1-8</sup> In this Perspective paper we concentrate on the particular application of the muon-spin rotation/relaxation technique for conducting experiments under the hydrostatic pressure conditions. The particular attention is paid to the description of the existing high-pressure muon facility at the Paul Scherrer Institute (PSI), Switzerland.

The paper is organized as follows. Section II comprises a short description of the  $\mu$ SR method. Particular attention is paid to the specificity of combination of the hydrostatic pressure and  $\mu$ SR techniques (Sec. II A). The muon implantation depth and the requirements for the  $\mu$ SR pressure cell construction are discussed in Sec. II B. The recent developments in  $\mu$ SR pressure instrumentation are presented in Sec. III. These include the description of the  $\mu$ E1 decay beam line (with the particular attention payed to the formation of the spin-rotated muon beam, Sec. III A); the upgraded version of the General Purpose Decay (GPD) muon spectrometer (Sec. III B); the construction of the three-wall piston-cylinder pressure cell (Sec. III C 2); and the optical setup for the in-situ pressure determination (Sec. III C 3). Few scientific examples showing the ability of  $\mu$ SR under pressure technique for studying the magnetism, superconductivity and the interplay between these two phenomena are discussed in Sec. IV.

## II. BASIC PRINCIPLES OF $\mu$ SR UNDER PRESSURE EXPERIMENTS

This Section discusses the basic principles of  $\mu$ SR under pressure experiments. The Section starts from the calculated muon stopping distribution inside the typical  $\mu$ SR pressure cell. The scattering of muons at the pressure cell walls sets limitations as for the energy of the implanted muons, so for the construction of the  $\mu$ SR pressure cells.

### A. The muon stopping inside the pressure cell

A schematic view of the  $\mu$ SR under pressure experimental setup is presented in Figure 1. The muons are implanted along the  $z$ -axis. The initial spin of incoming muons may stay nearly parallel (or antiparallel) to the muon momentum  $\mathbf{p}_\mu$ , or turned at angle  $\beta$  by using the so-called spin-rotator devices

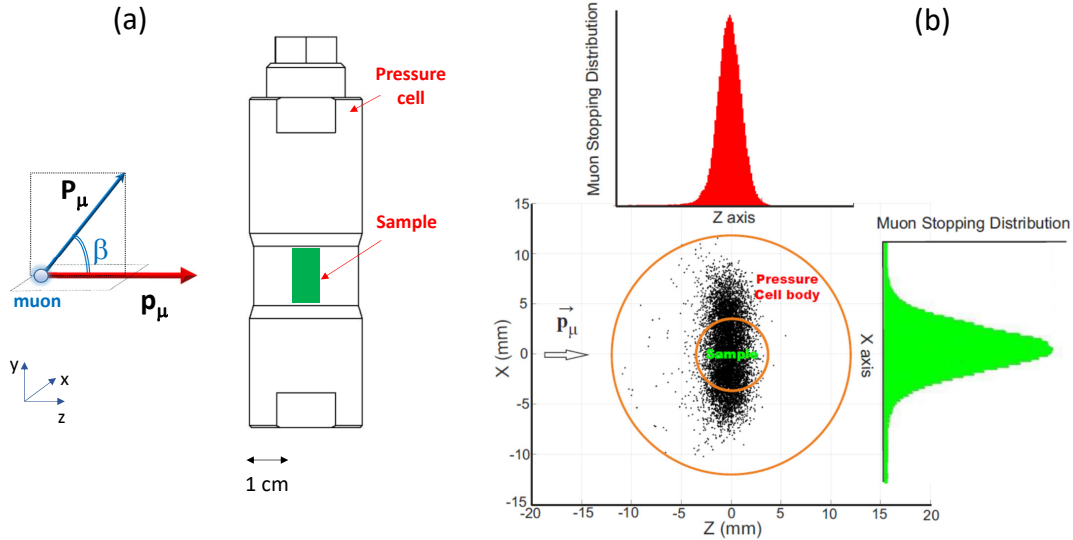


FIG. 1. (a) The schematic view of a cylindrical pressure cell (black contour) with the sample inside (green rectangular). The muons are implanted along the  $z$ -axis. The spin of incoming muons might be turned at angle  $\beta$  from the direction of the muon momentum  $\mathbf{p}_\mu$ . (b) The cross sectional view ( $x-z$ ) of the pressure cell. The colored areas represent the muon stopping distributions in parallel (red) and perpendicular (green) directions to the muon beam. The energy of implanted muons was set to 44 MeV. The simulations were performed by using TRIM.SP package, Ref. 22. The figure is adapted after Ref. 6.

(see Sec. III A 1 for different types of spin-rotated muons accessible at the decay muon beam lines). The  $\mu$ SR experiments could be conducted in different configurations, which are distinguished by an angle between the applied magnetic field and the initial muon-spin polarization of the incoming muon beam ( $\mathbf{P}_\mu$ ), as well as might be performed without applying field. The detailed description of the zero-, the transverse- and the longitudinal-field  $\mu$ SR experiments could be found in the following textbooks, Refs. 9–15, and review articles, Refs. 5, 16–21.

By entering the pressure cell, muons are scattered at the cell walls, so, by reaching the sample, the muon beam diverges in both, the parallel and the perpendicular directions to the muon beam. The cross sectional view of muons spread inside the pressure cell walls and the sample are presented in Figure 1 (b). The simulations were performed by using the TRIM.SP package for the pressure cell made of MP35N alloy (the outer and the sample diameters 24 and 6 mm, respectively) and for the muon beam width of 4 mm. The energy of implanted muons was set to 44 MeV.

### B. Muon implantation energy and the pressure cell construction

The results presented in Fig. 1 set limitations as for the energy of the implanted muons, so for a possible constructions of the  $\mu$ SR pressure cells. Indeed, by approaching the sample, the muon beam diverges quite substantially. The FWHM of the muon stopping distribution reaches  $\simeq 4$  and 8 mm in the parallel and perpendicular to the beam directions, respectively. Consequently, in order to stop substantial amount of muons inside the sample (*i.e.* not in the pressure cell walls),

the sample volume must be relatively high (of the order of few hundred cubic millimeters). At the same time, the pressure cell needs to be compact enough in order to fit into the cryogenic environment and the muon detector block. By following the 'maximum pressure' vs. 'sample volume' diagram presented by Klotz in Ref. 23, it becomes obvious that only the so-called piston-cylinder pressure cell construction satisfies such criteria.

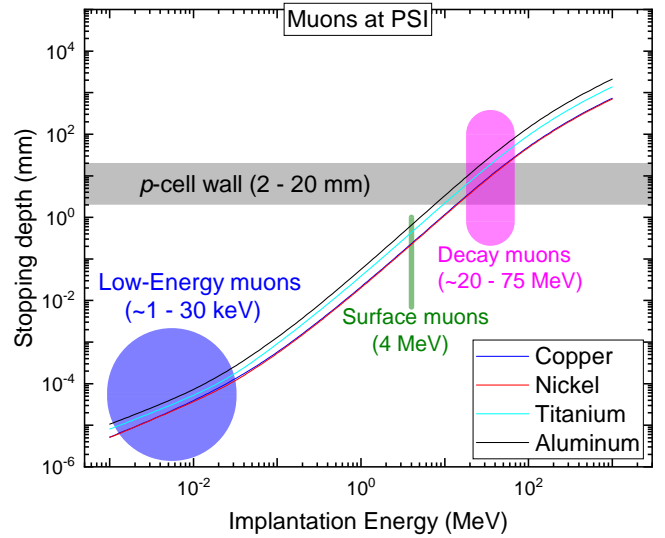


FIG. 2. Dependence of the mean stopping depth on the implantation energy for muons produced at various beam facilities at the Paul Scherrer institute. The calculations were performed by using TRIM.SP package, Ref. 22.

As for the energy of implanted muons. Figure 2 represents the dependence of the mean stopping depth as a function of the implantation energy for muons produced at various beam line facilities at the Paul Scherrer Institute (PSI). The calculations were performed for four different elemental metals, namely Copper, Nickel, Titanium and Aluminum. These metals are either used themselves as materials for the cells (as, *e.g.*, Aluminum), or enter various hard alloys as a main component (see, *e.g.*, Refs. 5, 6, 8, 23–25 and Table I in Sec. III C 1). The horizontal grey stripe corresponds to the pressure wall thickness ranging from 2 to 20 mm. Obviously, only the so called 'decay-muons', with the implantation energy ranging between  $\simeq 20$  and 75 MeV, become suitable for  $\mu$ SR under pressure studies.

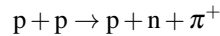
### III. INSTRUMENTATION

This Section provides an overview of the instrumentation used to perform  $\mu$ SR under pressure experiments at the Paul Scherrer Institute, Switzerland. The Section includes the description of the  $\mu$ E1 decay beam line (with the particular attention paid for the formation of the spin-rotated muon beam), the upgraded version of the General Purpose Decay (GPD) muon spectrometer, the construction of the three-wall piston-cylinder pressure cell and the optical setup for the in-situ pressure determination. The description of the old version of the GPD spectrometer, the double-wall piston cylinder pressure cells, and the way of the pressure determination by means of AC-susceptibility technique could be found in Refs. 5–7.

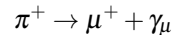
#### A. The $\mu$ E1 decay muon beam line

##### 1. The decay muon production

In a large scale facilities, like the one at PSI, the muon beams are produced from high energetic protons. Protons are collided into a target made of carbon, thus resulting in pions which further decay into muons. The two-step process of producing the positively charged muon beam could be described as:



for the pion and



for the muon production, respectively. Here  $p$ ,  $\pi$ ,  $\mu$ ,  $n$  and  $\gamma_\mu$  denote the proton, pion, muon, neutron and muon neutrino, respectively. The spin of the pion is zero and the muon neutrino has a definite helicity. This requires that within the reference frame of the pion the spin of the positively charged muon is aligned *oppositely* to the muon momentum.<sup>9–15</sup> Large-scale facilities can provide two type of muon beams, namely the 'surface' and the 'decay' ones. The description of the surface muon beam lines could be found in textbooks, Refs. 9–15, as well as in review articles, Refs. 16–20.

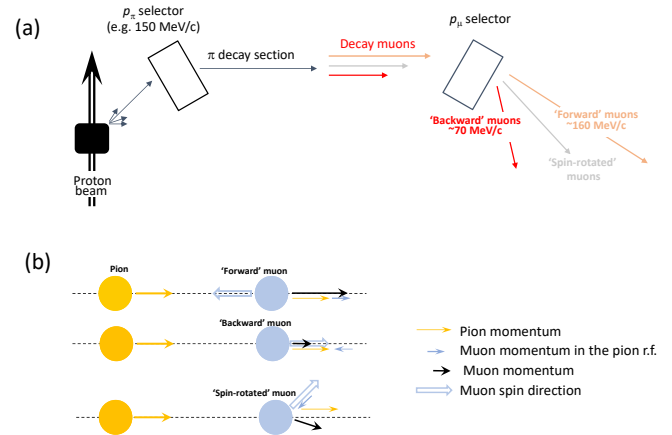


FIG. 3. (a) The schematic representation of the decay muon beam line. The high-energy pions are ejected from the target and transported down to a pion momentum selection element (' $p_\pi$  selector'). The pion decay occurs in flight inside the pion decay channel (' $\pi$  decay section'). The muon momentum selection part [' $p_\mu$  selector'] allows to choose muons with the desirable energy. (b) Three different types of decay muons which might be collected at the end of the pion decay section. The 'Forward' muons have the highest possible momentum and the muon-spin aligned opposite to the muon momentum. The 'Backward' muons have the smallest momentum and the spin aligned along the muon momentum. The 'Spin-rotated' muons are emitted at a certain angle from the beam line axis. The spin direction of such muons may, in principle, vary between 0 and 180 degrees.

Figure 3 (a) explains the working principles of a decay beam line. The high-energy pions are ejected from the target and transported down to a pion momentum selection element (' $p_\pi$  selector'). The pion decay occurs in flight inside the pion decay channel (' $\pi$  decay section'). It is important that the length of pion's trajectory within the decay channel should be comparable with the pion decay length. The muons, which are captured at the end of the pion decay section, might be further transported to the spectrometer. The muon momentum selection part [' $p_\mu$  selector'] allows to choose muons with the desirable energy.

It is important to emphasize here, that the decay beam lines allow to obtain muon beams with the different initial muon-spin polarization. This is opposed to the surface beam lines, where the muon-spin and the muon momentum are aligned oppositely (here we do not consider the presence of a Wien-filter based spin-rotation device). As is explained in Fig. 3 (b), the particular muon-spin polarization at the decay beam line would depend on the muon emission direction at the reference frame of the pion. In practice, two extreme conditions are commonly used:

1. The muon is emitted in the direction of the pion momentum, *i.e.* in the 'forward' direction [the top diagram in Fig. 3 (b)]. The resulting muon momentum (black arrow) consists of the muon momentum in the reference frame of the pion (blue thin arrow) and the momentum of the pion (yellow arrow). The final muon momentum of the 'forward' muon is, therefore, greater than the one

of the pion and the muon-spin points in the opposite direction of its propagation.

2. The muon is emitted in the direction opposite to the pion momentum, *i.e.* in the 'backward' direction [the middle diagram in Fig. 3 (b)]. The final muon momentum is smaller than that of pion. The muon spin is aligned along the muon momentum.

The intermediate case, *i.e.* muons with the muon-spin rotated at a certain angle from the main beam axis [the bottom diagram at Fig. 3 (b)] was not in use until recent. This is important configuration, however, since it allows to perform  $\mu$ SR experiments in the so-called spin-rotated mode. In such case:

3. The final momentum of the 'spin-rotated' muon becomes a vector sum of the pion and the muon momentum in the pion's reference frame [the lowest diagram in Fig. 3 (b)]. The spin of the muon is aligned opposite to the muon momentum in the reference frame of the pion and it stays, therefore, turned (rotated) at a certain angle from the beam trajectory. The absolute value of the muon momentum may stay in between values allowed for the 'forward' and 'backward' muon, respectively. Note that in such configuration the muon is emitted at an angle to the beam direction [see the black arrow at the lowest diagram of Fig. 3 (b)], so one needs certain modification of the beam transport in order to bring such muons back to the main trajectory. The first successful attempt of using the spin-rotated muons at the decay beam line was made at the M9B beam line at TRIUMF, Canada.<sup>26</sup>

## 2. $\mu$ E1 beam line with asymmetrically driven quadrupole magnet

The  $\mu$ E1 decay muon beam line installed at PSI was previously discussed in Ref. 5. The schematic view of the beam line is presented in Fig. 4. The 'beam optics' consist of various magnets used to transport the muon beam to the experimental measuring station. All magnets are tunable, thus allowing to control precisely both, the beam momentum and the beam spread. The magnets are either quadrupoles (red rectangles) or bending magnets (blue elements). The quadrupoles, which stay in a sequence of 2, 3 or 4 elements, are used to focus the muon beam, while the bending magnets play a role of momentum selection elements. Slits are used to limit the lateral beam extension and reduce the beam intensity.

The transport of the pion/muon beam occurs in the following way. The high-energy pions leave the 'Target E' at high energies. They are collected over a certain solid angle by quadrupole magnets. The bending magnet ASX81 plays a role of a pion momentum selector. The pion decay section consists of an 8 m long superconducting solenoid with a field of  $\simeq 5$  T. Pions decay before reaching the end of the solenoid, so the end of the solenoid section becomes a diffuse source of the muons. The selection of the muon momentum is performed

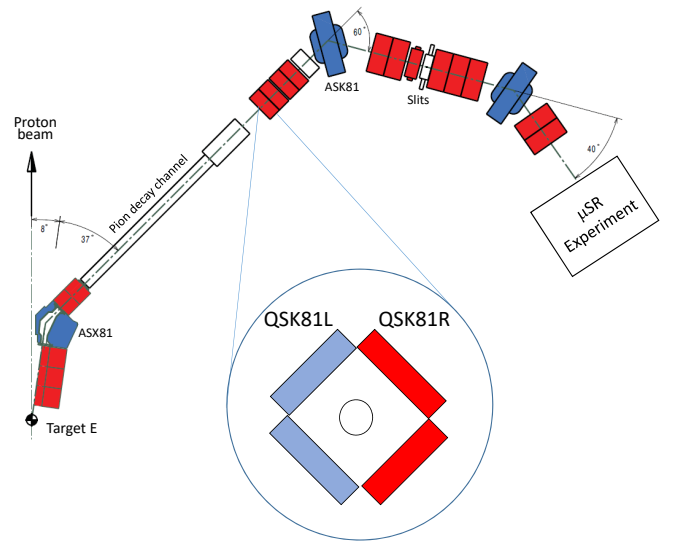


FIG. 4. The schematic view of the  $\mu$ E1 decay muon beam line at the Paul Scherrer Institute, Switzerland. The 'beam optics' consist of magnets used to transport the muon beam to the measuring station. The magnets are either quadrupoles (red rectangles) or bending magnets (blue elements). Slits are used to limit the lateral beam extension and reduce the beam intensity. The extension inside the circle represents the asymmetrically driven QSK81 quadrupole magnet. QSK81L and QSK81R stay for the 'left' and 'right' coils which are run by separate power supplies.

at the ASK81 bending magnet. The rest of the beam elements are used to transport muons to the experimental station.

All quadrupole magnets, except QSK81, are run 'symmetrically', *i.e.* currents flowing through all four magnet coils stay equal. This is a standard operational mode of a quadrupole magnet.<sup>27</sup> In order to collect the 'spin-rotated' muons [see Sec. III A 1 and Fig. 3 (b)] connections to QSK81, *i.e.* the first quadrupole magnet at the end of the pion decay channel, were modified. The 'left' (QSK81L) and the 'right' (QSK81R) pair of coils were run from separate power supplies (see the schematic representation of the magnet in Fig. 4). In such configuration the QSK81 magnet was allowed to operate in both, the 'symmetric' and the 'asymmetric' modes.

## 3. The muon-spin rotation at $\mu$ E1 beam line

The  $\mu$ E1 beam line, in its original design presented in Ref. 5, is capable to transport the 'forward' and the 'backward' muons [the top and the intermediate panels in Fig. 3 (b)]. In such configurations, the muon-spin is aligned either antiparallel or parallel to the muon momentum and it remains, therefore, 'non-rotated'. In order to collect the 'spin-rotated' muons, the first beam focusing element at the end of the pion decay section must be able to compensate for deviation of the muon momentum from the beam line axis [see the lowest panel at Fig. 3 (b)]. It requires for the QSK81 magnet to have both, the quadrupolar (focusing) and the dipolar (bending) components. This becomes possible by running the

quadrupolar QSK81 magnet in the above mentioned 'asymmetric' mode (see Sec. III A 2 and Fig. 4).

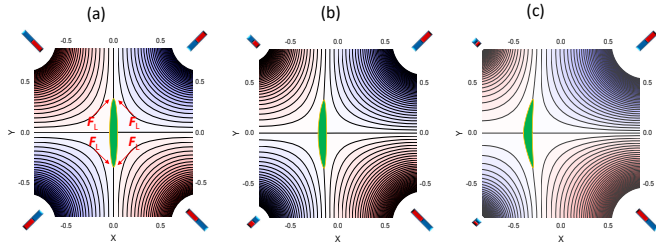


FIG. 5. (a) The equipotential magnetic field lines of a symmetrically driven quadrupole magnet. Arrows indicate directions of the Lorentz force. The green oval at the center represent the beam spot. The quadrupole focuses the beam horizontally and de-focuses it in the vertical direction. (b) and (c) The equipotential magnetic field lines of a quadrupole magnet in the asymmetric mode. The left pair of magnets is weaker compared to the right one. The appearance of the dipolar component, *i.e.* the shift of the beam spot from the central position in horizontal direction is clearly visible.

The simulations of an asymmetrically driven quadrupole magnet are presented in Fig. 5. Here, the poles of the quadrupole are modelled by four permanent magnets placed at corners. The solid lines represent the equipotential field surfaces. As expected, with all magnets being equal (*i.e.* in the symmetric case), the quadrupole focuses the beam of charged particles in one direction (horizontally) and de-focuses it in another direction (vertically), see Fig. 5 (a). By decreasing the magnetic field strengths of one pair of magnets [left pair in our case, Figs. 5 (b) and (c)], the beam spot slightly distorts and it shifts from the central position. Both, the dipolar and quadrupolar components, are clearly visible. One may also note the presence of the higher order components (sextuple, octuple *etc.*) which lead to small additional distortions of the beam-spot. These components, however, have a secondary importance and they are not considered here.

The resulting transversal-field  $\mu$ SR time spectra, accumulated after adjustment of the  $\mu$ E1 beam line for the 'spin-rotated' muon transport, are presented in Fig. 6. In these experiments the magnetic field 0.05 T [panel (a)], 0.1 T [panel (b)], and 0.2 T [panel (c)] was applied along the muon momentum [along the  $z$ -axis in Fig. 1 (a)]. The muon-spin rotation angle was estimated to be  $\beta \simeq 60^\circ$ . Note that this angle is comparable with the best muon-spin rotation device installed at the  $\pi$ M3 surface muon beam line at PSI.<sup>18</sup>

At the end of this Section the following three important points need to be mentioned:

- The decay beam lines allow to collect and transport the 'spin-rotated' muons down to the measuring station. The amount of the spin-rotated muons transported down to the sample is high enough to perform  $\mu$ SR under pressure experiments in the time differential mode ( $\sim 35 \cdot 10^3$  muons per second down to the muon momentum  $p_\mu \simeq 90$  MeV/c).
- The major element allowing to capture the spin-rotated muons is the asymmetrically driven quadrupole, where

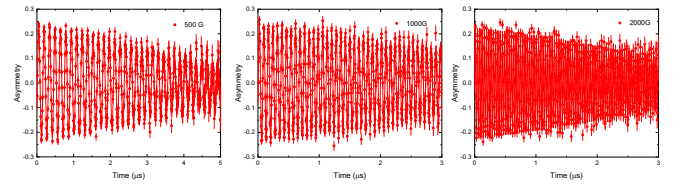


FIG. 6. (a) The muon-time spectra collected by using the spin-rotated muon beam at the  $\mu$ E1 beam line. The external magnetic field  $\mu_0 H = 0.05$  T is applied parallel to the muon momentum [along the  $z$ -axis in Fig. 1 (a)]. The muon momentum is kept at 100 meV/c. (b) and (c) The same as in panel (a) but for  $\mu_0 H = 0.1$  T and 0.2 T, respectively.

both, the quadrupolar (focusing) and the dipolar (bending), components are present.

- The rotation of the muon-spin occurs without use of the so-called Wien-filter setup as is performed, *e.g.*, at the 'surface' and the low-energy muon beam lines.<sup>28,29</sup>

## B. The General Purpose Decay (GPD) $\mu$ SR spectrometer

The GPD (General Purpose Decay)  $\mu$ SR spectrometer is permanently installed at the end of the  $\mu$ E1 beam line (see Sec. III A 2 and Fig. 4). The previous version of the GPD muon instrument was described in Ref. 5. The detector part was built using an old technology with the use of photomultiplier tubes and plastic light guides.

The new GPD detectors were built by using the silicon photomultipliers (SiPM's). The SiPM based  $\mu$ SR detectors deliver performances similar to that of photomultiplier tubes, Refs 28, 30–34, but they are also compact and insensitive to the magnetic field. These allows to mount the SiPM chips directly on the scintillator part of the detector [see, *e.g.*, Ref. 28 and Fig. 7 (a)]. The SiPM based  $\mu$ SR detectors were first developed to equip the avoided level-crossing instrument (ALC).<sup>30,31</sup> Later on, the similarly build detectors were used at the high magnetic field instrument HAL-9500,<sup>32,33</sup> the low-energy muon instrument (LEM),<sup>34</sup> and the General Purpose Surface (GPS) spectrometer,<sup>28</sup> all instruments stay at PSI.

In prior of upgrading the GPD instrument, the design and the efficiency of a new detector system were simulated by using the *musrSim* and *musrSimAna* software packages.<sup>35</sup> These software packages were successfully used to simulate several  $\mu$ SR instruments.<sup>28,32,36</sup> The *musrSim* program, based on the Geant4,<sup>37,38</sup> and Root packages,<sup>39</sup> calculates the detectors response to the muons and their decay products. The output of *musrSim* was further analysed with the general  $\mu$ SR analysis tool, *musrSimAna*. The subsequent use of these packages allows to implement the full logic of a real  $\mu$ SR experiment, as the coincidences and anti-coincidences between different detectors, as well as to obtain the time-independent background of the detector histograms. The reliability of the simulations were further tested by comparing the measured and simulated parameter values.

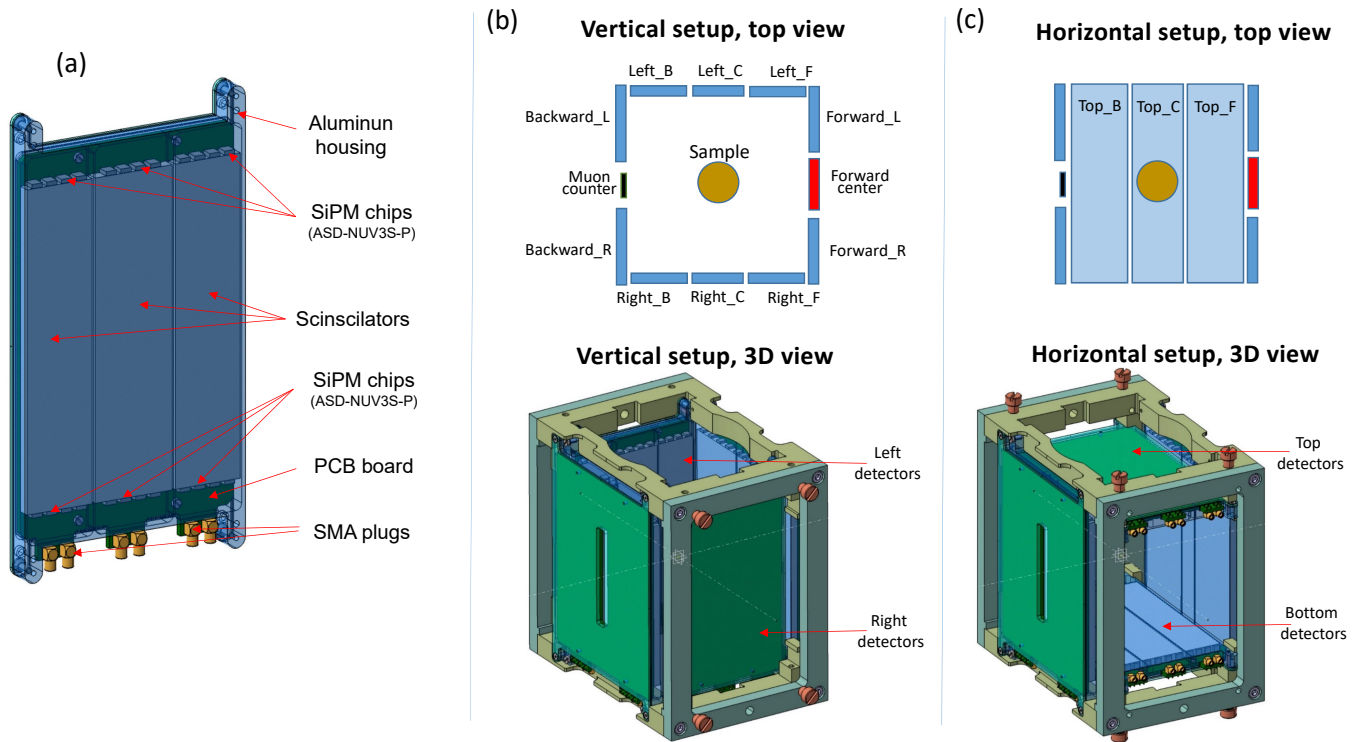


FIG. 7. (a) Construction of a SiPM based detector unit. The full block consists of three detectors. For each individual detector, the light from the scintillator is read-out on two opposite sites by arrays of 4 SiPM's (ASD-NUV3S-P) mounted on a printed electronics board and glued directly onto the scintillator material. (b) The 'vertical setup' of the GPD detector head. (c) The 'horizontal setup' of the GPD detector head. The change between the 'vertical' and the 'horizontal' setups is occurred by remounting the 'Left' and 'Right' detector units onto the 'Top' and the 'Bottom' positions, respectively

Figure 7 (a) demonstrates the construction of one SiPM based GPD detector unit. The single block, placed inside the light-tightened Aluminum housing, consists of three detectors. For each individual detector, the light from the scintillator is read-out on two opposite sites by arrays of 4 SiPM's (ASD-NUV3S-P from AdvanSiD, Ref. 40) mounted on a printed electronics board and glued directly onto the scintillator material. SiPM's are powered by a PSI-homemade multi-channel power supply (PSI HVR800). The analog signals from SiPM's are amplified by broadband amplifiers.<sup>33,41</sup> The output of the amplifiers are processed by constant fraction discriminators (PSI CFD-950, Ref. 42) and the signals are finally sent to a time-to-digital converter (CAEN, TDC V1190B). The event time for the incoming positron(muon) is calculated from the average time between the events recorded on both opposite edges.

Figures 7 (b) and (c) show two possible layouts of the GPD detector head, which are different by the cryostat's accessing directions and the detector's logic. The 'vertical setup' is used for cryostats loaded from the top [Fig. 7 (b)], while the 'horizontal setup' allows accessing from the side [Fig. 7 (c)]. The change between the setups is made by remounting the 'Left' and 'Right' detector units onto the 'Top' and the 'Bottom' positions, respectively [see the lower panels at Figs. 7 (b) and (c)].

As for the detector's logic. In both configurations the

'Backward' and the 'Forward' outputs are formed similarly. The positrons accumulated at the 'Backward\_L' and 'Backward\_R' detectors are summed together by forming a single 'Backward' output:  $\text{Backward} = \text{Backward}_L + \text{Backward}_R$ . The 'Forward' output is formed by either coupling all three detectors ( $\text{Forward} = \text{Forward}_L + \text{Forward center} + \text{Forward}_R$ ), or by coupling only two of them ( $\text{Forward} = \text{Forward}_L + \text{Forward}_R$ ) and leaving the 'Forward center' one as a so-called veto counter. Note that the veto mode is generally used to reject the muons missing the sample (see, *e.g.*, Ref. 28 for explanation of the veto principle).

As for the 'Left'/'Top' and 'Right'/'Bottom' set of detectors. Within the 'vertical setup' the coupling occurs for the opposed sections of the 'Left' and 'Right' detector units. The corresponding output channels are:  $\text{Backward}_{LR} = \text{Left}_B + \text{Right}_B$ ,  $\text{Center}_{LR} = \text{Left}_C + \text{Right}_C$  and  $\text{Forward}_{LR} = \text{Left}_F + \text{Right}_F$ , respectively. Note that, due to the highly asymmetric emission of the decay positrons, the 'Backward\_{LR}' and the 'Forward\_{LR}' channels accounts for nearly 60-65% of the initial muon-spin polarization and, because of this, they might be involved into the data analysis process. Within the 'Horizontal setup' the individual detectors in the 'Top' and 'Bottom' sections are coupled together by forming a large top ( $\text{Top} = \text{Top}_B + \text{Top}_C + \text{Top}_F$ ) and bottom ( $\text{Bottom} = \text{Bottom}_B + \text{Bottom}_C + \text{Bottom}_F$ ) positron

counters, respectively.

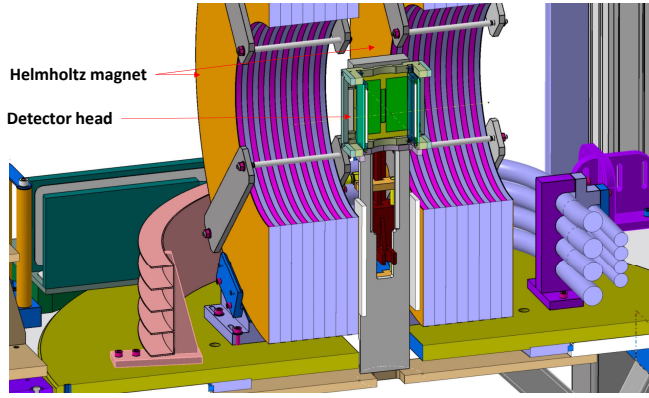


FIG. 8. The SiPM based detector head mounted on the GPD instrument platform.

The dimensions of the detector head (with all the detector units screwed together) is approximately  $12 \times 14 \times 15 \text{ cm}^3$ . Figure 8 demonstrates the mounting of the detector head inside the Helmholtz magnet, which is fixed to the GPD platform (see also Ref. 5 describing the construction of the old version of the GPD instrument).

### C. $\mu$ SR pressure cells

In this Section the construction materials, the design of the three-wall  $\mu$ SR pressure cell, and the optical setup for determining pressure inside the piston-cylinder cells are discussed. The single and the double-wall  $\mu$ SR pressure cell construction, as well as a way of pressure determination by means of AC susceptibility technique were presented in Refs. 3, 5, 6, and 43.

#### 1. The construction materials

By entering the cell muons are scattered at the pressure cell walls, so by reaching the sample the muon beam diverges in both, the transversal and longitudinal directions. The simulations presented in Fig. 1 (b) imply that substantial amount of muons stop in the pressure cell wall(s). This requires that the construction materials, which are used to build the cells, must have a low or, at best, the magnetic field and the temperature independent  $\mu$ SR background response. They should be also nonmagnetic, otherwise the induced magnetism at the cell walls may affect the sample response.

Materials used to build piston-cylinder pressure cells should be distinguished between materials suitable for the pressure cell body and that for the compressive pistons. Obviously, the body of the cell should be able to withstand both, the compressive and tensile type of deformations, while pistons should resist against very high compressions.

Table I summarizes the list of nonmagnetic alloys, which might be used to build bodies of  $\mu$ SR cells. For such mate-

rials the most relevant parameters are: the yield strength (the maximum strength up to which material responds elastically,  $\sigma_Y$ ), the Young modulus (the slope of the linear part of the stress-strain curve for a material under tension/compression,  $E$ ) and ductility (a measure of a material's ability to undergo significant deformation before rupture or breaking,  $\Delta l/l$ ). The rest of the mechanical parameters, as well the mechanical and thermal treatment procedures, could be found at the corresponding producers web sites and some pressure technique dedicated papers and books (see, *e.g.*, Ref. 23–25).

TABLE I. The yield strengths ( $\sigma_Y$ ), Young modulus ( $E$ ) and ductility ( $\Delta l/l$ ) for some nonmagnetic alloys, which could be used to build the  $\mu$ SR pressure cell bodies. The values of  $\sigma_Y$ ,  $E$ , and  $\Delta l/l$  are given for  $T \simeq 300 \text{ K}$ . The meaning of the alloys: Al-7075 – aluminum alloy; TAV6 – titanium alloy containing 90 wt.% Ti, 4 wt.% Al, and 6 wt.% V; CuBe – beryllium copper (Berylico-25); NiCrAl – nickel based alloy containing 57 wt.% Ni, 40 wt.% Cr, and 3 wt.% Al; MP35N – Ni/Co based alloy containing 35 wt.% Ni, 35 wt.% Co, 20 wt.% Cr, and 10 wt.% Mo. All materials are aged to the optimum conditions allowing to get maximum possible value of the Yield strengths.<sup>23–25</sup>

	Al-7075	TAV6	CuBe	NiCrAl	MP35N
$\sigma_Y$ (GPa)	0.5	1.05	1.3	2.06	2.15
$E$ (GPa)	71.7	97	131	190	215
$\Delta l/l$ (%)	7	12	5	4-5	9

The pistons should withstand high compressive strength, which may allow the use of sintered compounds. The list of materials suitable to for producing nonmagnetic pistons are summarised in Table II.

TABLE II. The compressive strengths ( $\sigma_Y$ ) and the Young modulus ( $E$ ) for selected sintered compounds. The values of  $\sigma_Y$  and  $E$  are given for  $T \simeq 300 \text{ K}$ .<sup>23–25</sup>

	ZrO <sub>2</sub> -Y <sub>2</sub> O <sub>3</sub>	Al <sub>2</sub> O <sub>3</sub> -ZrO <sub>2</sub>	Si <sub>3</sub> N <sub>4</sub>	SiC	WC
$\sigma_Y$ (GPa)	2.2	4.7	5.1	8.3	5.0-11.0
$E$ (GPa)	210	357	241	918	600-670

The  $\mu$ SR pressure cells used at the Paul Scherrer Institute are made by using the CuBe, NiCrAl and MP35N nonmagnetic alloys. The pistons are made of Yttrium stabilized zirconia oxide (ZrO<sub>2</sub>-Y<sub>2</sub>O<sub>3</sub>), silicium nitride (Si<sub>3</sub>N<sub>4</sub>), or nickel binded tungsten carbide (WC). The  $\mu$ SR response of some of the above mentioned alloys and ceramic materials could be found in Refs. 3, 5, 6, and 44

#### 2. Three-wall pressure cell

The way of increasing the maximum reachable pressure in piston-cylinder cells is the use of the so-called compound

cylinder design. In such case the cells are made of two (or more) monobloc cylinders which are shrink fitted into each other.<sup>5,6,8,23–25,45</sup> The radial cross section of the single-wall (*s*), the double-wall (*d*), and the three-wall (*t*) cylinders are presented in Fig. 9. Here *a* and *b* are the inner and the outer diameters of the cylinder assembly, while *c*, *c*<sub>1</sub>, and *c*<sub>2</sub> are the diameters of the inner cylinders. For each particular geometry, the maximum pressures could be determined based on Lamé equations, see, *e.g.*, Refs. 23, 44, and 45. The maximum pressure values depend on the mechanical properties of the material (mostly on the yield strengths  $\sigma_Y$ , see Table I), the interface pressure between the cylinders, and the ratios of the cylinder diameters. Considering the optimum interface pressures, and assuming that all cylinders are made of the same materials, the Lamé equations result in maximum pressures as they presented at the lower part of Fig. 9.

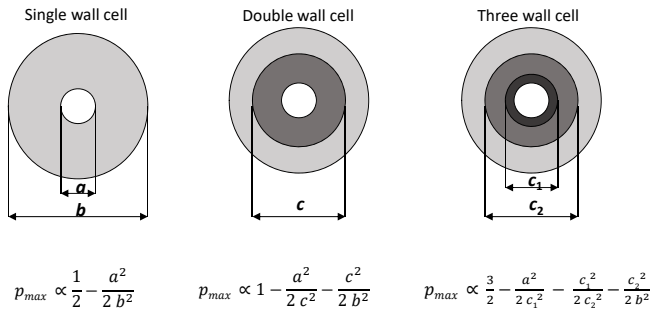


FIG. 9. The radial cross-section of the single-wall, the double-wall, and the three-wall compound cylinders. *a* and *b* are the inner and the outer diameters of the cylinder assembly. *c*, *c*<sub>1</sub>, and *c*<sub>2</sub> are the diameters of the inner cylinders. Equations represent maximum pressures for each particular cylinder geometry.

For the compound cylinder with *a* = 6 mm and *b* = 24 mm, which are typical dimensions for the pressure cells used in  $\mu$ SR experiments,<sup>5,6</sup> one gets:<sup>8</sup>

$$p_{\max}^s \div p_{\max}^d \div p_{\max}^t \simeq 1 \div 1.6 \div 1.92. \quad (1)$$

This suggests that the three-wall assembly allows to almost double the maximum pressure compared to the single-wall design and reaches  $\simeq 20\%$  higher values compared to the double-wall geometry.

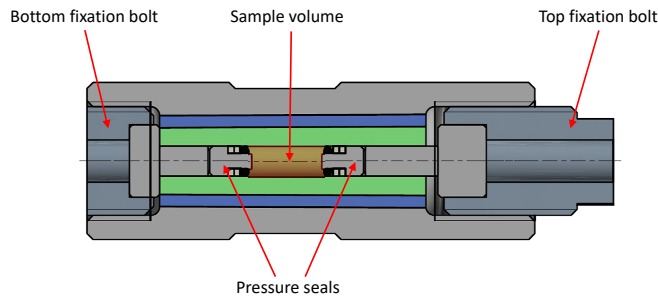


FIG. 10. The cross-sectional of the three-wall pressure cell. After Ref. 8.

The first attempt to build the three-wall pressure cell for

$\mu$ SR experiments is reported in Ref. 8. The mechanical drawing of the assembled three-wall pressure cell is shown in Fig. 10. The outer cylinder of the cell body was made from MP35N, while the middle and the inner cylinders were made from NiCrAl nonmagnetic alloys. The mechanical design and performance of the pressure cell were evaluated and optimised using finite-element analysis. The outcomes of the experimental testing closely match the modelling results. The three-wall  $\mu$ SR cell was shown to reach pressures of up to  $\simeq 3.3$  GPa at ambient temperature, corresponding to  $\simeq 3.0$  GPa at low temperatures, without irreversible damage.

### 3. Double volume pressure cell for optical pressure determination

Measurement of the absolute value of the pressure inside the piston-cylinder clamp cells used in  $\mu$ SR experiments is a complicated task. Until present, the pressure inside the  $\mu$ SR cell was determined via the AC susceptibility measurements by monitoring the pressure-dependent shift of the superconducting transition temperature ( $T_c$ ) of a small piece of elemental metal (In, Sn, or Pb).<sup>3,5,6,8</sup> This method has some disadvantages since: (i) the piece of the superconducting metal (the pressure indicator) stays in the close vicinity to the sample and it may affect the sample response, (ii) the pressure indicator occupies part of the sample volume and (iii) the absolute value of pressure measured just at a single temperature, which corresponds to  $T_c$  of the pressure indicator (below  $\sim 7$  K).

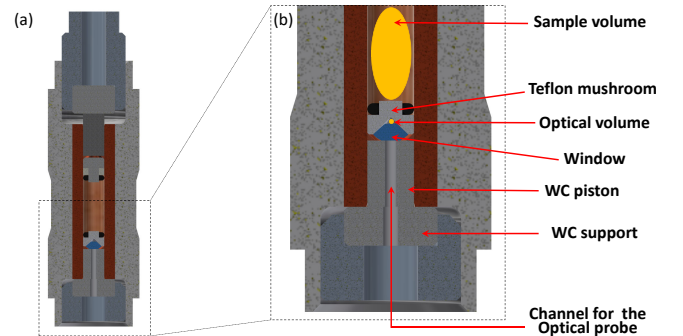


FIG. 11. (a) The cross-sectional view of the double-volume piston-cylinder pressure cell. The pressure cell body (with the inner and the outer diameters  $\varnothing 6$  and  $\varnothing 24$  mm, respectively) and the top part of the pressure seal [the mushroom, the tungsten carbide (WC) piston, the WC support, and the fixation bolt] are the same as they described in Refs. 5, 6, and 8. (b) The expanded part of the cell with the optical setup. The main elements are: the teflon mushroom with the conical entrance, the optical window prepared from the commercial gem crystal with the ‘brilliant-cut’ shape, and the WC piston with the entrance for optical fibers. The small and the big ovals represents volumes available for the sample and the optical probe, respectively. After Ref. 7.

In order to monitor the pressure inside the cell without reducing the volume available for the sample, as well as to prevent an influence of the pressure indicator material on the sample space, the concept of a double-volume pressure cell,



where the 'optical' and the 'sample' volumes are physically separated from each other, was developed and successfully tested in Ref. 7. As indicated in Fig. 11, the construction of the piston-cylinder cell was modified by introducing the tungsten carbide piston with the entrance for the optical fibers, the teflon seal with the conical cavity for an optical pressure indicator, and the optical window made of commercially available cubic-Zirconia single crystals. The technique developed in Ref. 7 allows to determine pressure inside the cell with the accuracy better than 0.01 GPa and might be potentially used to monitor the pressure inside the cell within the full temperature range allowed at GPD spectrometer (from  $\simeq 0.25$  K and up to the room temperature).

#### IV. SCIENTIFIC EXAMPLES

Muon spin rotation/relaxation might be applied for studying magnetic materials due to its high sensitivity to small fields and capability to probe both the static and dynamic local field distributions. ZF- $\mu$ SR is used to investigate microscopic magnetic properties of solids.<sup>5,9-21</sup> It also provides information on coexisting and competing phases in a material.<sup>46-52</sup> This is because muons stop uniformly throughout a sample, and the amplitudes of the  $\mu$ SR signals arising from the different regions of the sample are proportional to the volume occupied by a particular phase.

The transverse-field  $\mu$ SR is widely used to probe the important length scales of superconductors, namely the magnetic penetration depth  $\lambda$  and the coherence length  $\xi$ .<sup>5,11,13-16,20,21</sup> Experiments in the vortex state of a type II superconductor allow to determine  $\lambda$  in the bulk of the sample, in contrast to many techniques that probe  $\lambda$  only near the surface. The penetration depth  $\lambda$  is one of the fundamental parameters of a superconductor, since it is related to the density of superconducting carries ( $n_s$ ) and the supercarrier mass ( $m^*$ ) by the London equation  $1/\lambda^2 = \mu_0 n_s e^2 / m^*$ . The functional form of  $n_s(T)$  depends on the gap symmetry and may bring direct information on the presence of multiple superconducting energy gaps.<sup>21,53-57</sup>

A high sensitivity of  $\mu$ SR to internal fields makes it an extremely important for studying effects of time reversal symmetry breaking (TRSB). Superconducting states with broken time reversal symmetry have Cooper pairs with non-zero magnetic moments.<sup>43,58-64</sup> The TRSB charge density wave (CDW) order is characterized by carriers flowing over the closed loops which also leads to appearance of a small moments. In both, the TRSB superconducting<sup>43,58-64</sup> and TRSB CDW states,<sup>65-69</sup> a local alignment of these moments results in extremely small internal magnetic fields which might be probed by ZF- $\mu$ SR technique.

In the following, we present a few selected experimental results obtained by performing  $\mu$ SR under pressure experiments. For further details and examples we refer to the original articles which were published during the last five years, Refs. 6-8, 43, 47-57, 70-91 and those mentioned in the previous review paper, Ref. 5.

#### A. The high-pressure magnetic state of MnP

The pressure-temperature phase diagram of MnP was found to be rather complex. By starting from ambient pressure, MnP obeys couple of magnetic transitions, with the last currently 'unknown' magnetic phase becoming a precursor of the superconductivity.<sup>92</sup> The superconducting dome with the maximum transition temperature  $T_c \approx 1$  K emerges near the pressure  $p \simeq 8$  GPa, where the long-range magnetic order vanishes.<sup>92</sup>

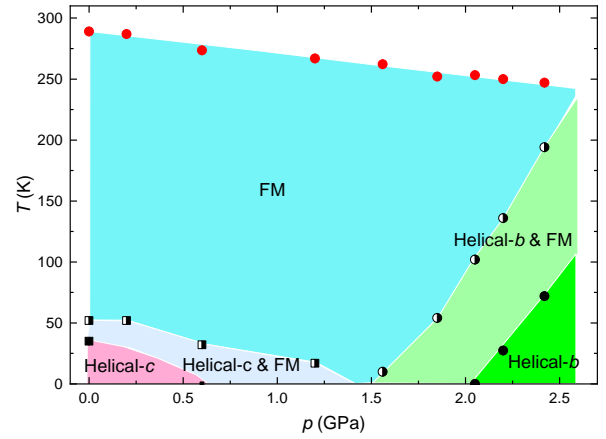


FIG. 12. (a) The  $p - T$  phase diagram of MnP obtained from  $\mu$ SR experiments. FM, Helical- $c$ , and Helical- $b$  denote different types of magnetic order (see the main text and Refs. 48 and 49). The half filled and filled symbols correspond to the case when the helical- $c$  (pink squares) or the helical- $b$  (blue circles) phases occupy 10% and 90% of the sample volume, respectively. After Refs. 48 and 49

In view of its ability to provide an additional microscopic information on the magnetic and the superconducting properties of MnP,  $\mu$ SR studies under applied hydrostatic pressure were conducted.<sup>48,49</sup> The resulting  $p - T$  phase diagram consists of three areas corresponding to the ferromagnetic (FM), helical- $c$  and helical- $b$  magnetic orders (see Fig. 12). The phases FM/Helical- $c$  as well as FM/Helical- $b$  are found to coexist within broad range of pressures and temperatures. Transitions from the high-temperature FM to the low-temperature low-pressure helical- $c$ , or the low-temperature high-pressure helical- $b$  phases are first-order like. These experiments appear to confirm that in MnP the high-pressure magnetic phase which is the precursor of the superconducting state is the incommensurate helical- $b$  type.

#### B. Pressure Dependence of the Superfluid Density in the Nodeless Topological Superconductor $\alpha$ -PdBi<sub>2</sub>

The  $\mu$ SR experiments performed on a topological superconductor candidate  $\alpha$ -PdBi<sub>2</sub> have suggested the absence of any nodes in the superconducting gap structure of this compound, and were found to be best described by a fully gapped  $s$ -wave model.<sup>88</sup> Observation of  $s$ -wave superconductivity in this system along with its unique band structure and Fermi

surface topology endorse this compound as a promising candidate in the search for Majorana zero modes. The superconducting gap value and the superfluid density were found to decrease with increasing pressure up to  $p \simeq 1.77$  GPa. The most intriguing observation of  $\mu$ SR under pressure studies is the linear dependence between  $T_c$  and the superfluid density manifesting an unconventional superconductivity in this compound.

### C. Unsplit superconducting and time-reversal symmetry breaking transitions in $\text{Sr}_2\text{RuO}_4$ under hydrostatic pressure and disorder.

For a long time  $\text{Sr}_2\text{RuO}_4$  was considered to be a rear example of  $p_x \pm ip_y$  triplet chiral superconductors.<sup>93–97</sup> Such conclusion was based on observation of a TRSB superconducting state in the ZF- $\mu$ SR<sup>58</sup> and polar Kerr effect data,<sup>98</sup> as well as on the absence of suppression of the NMR Knight below the superconducting transition temperature.<sup>99</sup> The chirality was also supported by the phenomenology of junctions between  $\text{Sr}_2\text{RuO}_4$  and conventional superconductors evidencing for existence of domains within the superconducting state.<sup>100,101</sup> However, the triplet superconductivity was found to stay in conflict with the strain dependence of the upper critical field,<sup>102</sup> and the recent revision of NMR data on unstrained  $\text{Sr}_2\text{RuO}_4$ .<sup>103,104</sup>

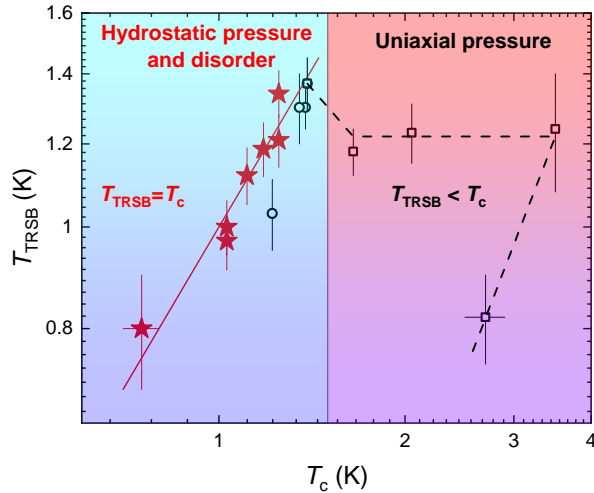


FIG. 13. Dependence of the time-reversal symmetry-breaking temperature  $T_{\text{TRSB}}$  on the superconducting transition temperature  $T_c$  for  $\text{Sr}_2\text{RuO}_4$ .<sup>43</sup> The colored areas represents parts with the preserved tetragonal lattice symmetry (hydrostatic pressure and disorder effects) and with orthorhombic distortions in the lattice (uniaxial pressure). The red solid line corresponds to  $T_{\text{TRSB}} = T_c$ . The dashed line is the guide for the eye.

It was expected that the lattice-symmetry preserved hydrostatic pressure and disorder with an isotropic in-plane scattering potential can not split  $T_c$  and the TRSB transition temperature ( $T_{\text{TRSB}}$ ), while strong splitting between  $T_c$  and  $T_{\text{TRSB}}$  are expected for the perturbations braking the crystallographic

symmetry. The recent  $\mu$ SR experiments reveal that the superconducting and TRSB transitions do not split under hydrostatic pressure up to 0.95GPa in pure  $\text{Sr}_2\text{RuO}_4$  and in the La doped  $\text{Sr}_{2-x}\text{La}_x\text{RuO}_4$  sample with  $T_c \approx 0.7\text{K}$  (see Fig. 13).<sup>43,63</sup> These results provide evidence in favor of a chiral superconductivity in  $\text{Sr}_2\text{RuO}_4$ .

### D. Universal relations for type-I superconductors

For type-I superconductors the famous empirical trend, as reported by Rohlf in Ref. 105, is the linear relation between the zero-temperature value of the thermodynamic critical field  $B_c(0)$  and the transition temperature  $T_c$ , see Fig. 14. The fact, that the critical magnetic field required to destroy the superconducting state is strongly correlated with the critical temperature, suggests that each of these parameters can be viewed as representative of energy, which can be supplied to the material in such a way that it interferes with the superconducting mechanism. This is consistent with the idea that there is a bandgap between the superconducting and normal states. The proportionality between  $T_c$  and the superconducting gap is a well accepted issue, however it is not clear why  $B_c(0)$  should follow the similar trend.

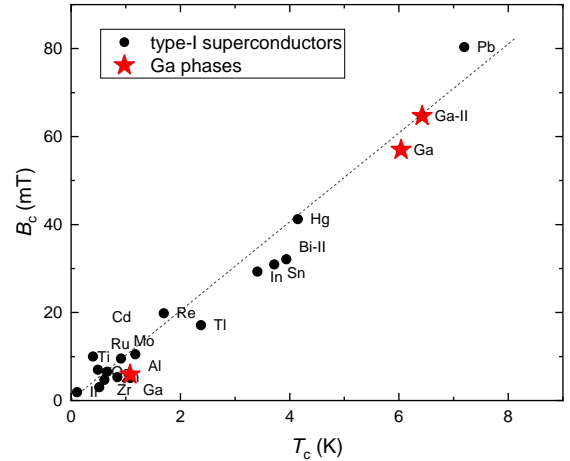


FIG. 14. The empirical relation between the zero-temperature value of the thermodynamic critical field  $B_c(0)$  and the transition temperature  $T_c$  for type-I superconductors, after Rohlf, Ref. 105. Black symbols are data points from Refs. 90, 91, 106–115. Red stars correspond to different Gallium phases from Refs. 89, 106, and 110. After Ref. 89.

In view of its ability to detect superconducting responses,  $\mu$ SR studies of the pressure induced Gallium-II phase of the elemental gallium were conducted, Ref. 89. The correlations between the coupling strength  $2\Delta/k_B T_c$  ( $\Delta$  is the superconducting gap), the ratio  $B_c(0)/T_c \sqrt{\gamma_e}$  ( $\gamma_e$  is the electronic specific heat), and the specific heat jump at  $T_c$ ,  $\Delta C(T_c)/\gamma_e T_c$  was shown to exist in phonon-mediated superconductors. Such correlations were naturally explaining the linear relation between  $B_c(0)$  and  $T_c$ , as well as give an estimate of  $B_c(0)/T_c$  ratio.

## V. OUTLOOK

The muon-spin rotation/relaxation ( $\mu$ SR) measurements provide an insight into how the muon interacts with its local environment. From this, unique information is obtained about the static and dynamic properties of the material of interest. This Perspective paper concentrates on the particular application of the  $\mu$ SR technique for conducting experiments under the hydrostatic pressure conditions. The main attention was paid to the description of the existing high-pressure muon facility at the Paul Scherrer Institute (PSI), Switzerland.

Further possible development of PSI's  $\mu$ SR pressure facility may be classified along three lines. First, a new fiber reading system is planned to be installed in several cryostats during the next few years. The use of such system would allow to monitor the pressure value within a full temperature range studied and, by doing this, to the more accurate determination of the sample properties. The second part relates to the improvement of the  $\mu$ SR pressure cells. This includes: (i) the search for a new strong materials which might be suitable for building the  $\mu$ SR cells; (ii) the investigation of a new pressure cell designs, as, e.g., the McWhan-type cells, belt-type cells, three-wall cells, etc.; and (iii) the possible use of an anvil-type of design. The third part is tend to development of the in-situ press system, which may allow to change the pressure inside the cell directly at the muon instrument.

## ACKNOWLEDGMENTS

The author would like to thank Matthias Elender, Alex Amato, Elvezio Morenzoni, Hubetrus Luetkens, Zurab Guguchia, Ritu Gupta, Debarchan Das, Kamil Sedlak, Gediminas Simutis, Hans-Ruedi Walter, Alexey Stoykov, Andrea Raselli, Kontstantin Kamenev, Stefan Klotz, Davide Reggiani, Thomas Rauber, Pavel Naumov, and Marek Bartkowiak for their help and for making the  $\mu$ SR under pressure project to be running successfully.

- <sup>1</sup>T. Butz, G.M. Kalvius, B. Lindgren, O. Hartmann, R. Wäppling, and E. Karlsson, *A high pressure, low temperature system for  $\mu$ SR studies*, *Hyp. Interact.* **32**, 881 (1986).  
doi: 10.1007/BF02394998
- <sup>2</sup>A. Kratzer, K. Mutzbauer, S. Heuneberger, G.M. Kalvius, O. Hartmann, R. Wäppling, H.H. Klauß, M.A.C. de Melo, E.J. Litterst, and T. Stammel, *High pressure  $\mu$ SR studies*, *Hyp. Interact.* **87**, 1055 (1994).  
doi: 10.1007/BF02068504
- <sup>3</sup>D. Andreica, Ph. D. Thesis, IPP/ETH-Zürich, 2001.
- <sup>4</sup>I. Watanabe, Y. Ishii, T. Kawamata, T. Suzuki, F.L. Pratt, R. Done, M. Chowdhury, C. Goodway, J. Dreyer, C. Smith, and M. Southern, *Development of a gas-pressurized high-pressure  $\mu$ SR setup at the RIKEN-RAL Muon Facility*. *Physica B.* **404**, 993 (2009).  
doi: 10.1016/j.physb.2008.11.209
- <sup>5</sup>R. Khasanov, Z. Guguchia, A. Maisuradze, D. Andreica, M. Elender, A. Raselli, Z. Shermadini, T. Goko, F. Knecht, E. Morenzoni, and A. Amato, *High pressure research using muons at the Paul Scherrer Institute*, *High Pressure Research* **36**, 140 (2016).  
doi: 10.1080/08957959.2016.1173690
- <sup>6</sup>Z. Shermadini, R. Khasanov, M. Elender, G. Simutis, Z. Guguchia, K. V. Kamenev, and A. Amato, *A low-background piston-cylinder type hybrid high pressure cell for muon-spin rotation/relaxation experiments*. *High*

- Pressure Research* **37**, 449 (2017).  
doi: 10.1080/08957959.2017.1373773
- <sup>7</sup>P. Naumov, R. Gupta, M. Bartkowiak, E. Pomjakushina, N. P. M. Casati, M. Elender, and R. Khasanov, *Optical Setup for a Piston-Cylinder Pressure Cell: A Two-Volume Approach*. *Phys. Rev. Applied* **17**, 024065 (2022).  
doi: 10.1103/PhysRevApplied.17.024065
- <sup>8</sup>R. Khasanov, R. Urquhart, M. Elender, and K. Kamenev, *Three-wall piston-cylinder type pressure cell for muon-spin rotation/relaxation experiments*. *High Pressure Research*, **42**, 29 (2022).  
doi: 10.1080/08957959.2021.2013835
- <sup>9</sup>A. Schenck, *Muon Spin Rotation Spectroscopy: Principles and Applications in Solid State Physics*. Adam Hilger, Bristol, 1985.
- <sup>10</sup>A. Schenck and F.N. Gygax, *Magnetic Materials Studied by Muon Spin Rotation Spectroscopy*. in: *Handbook of Magnetic Materials*, edited by K.H.J. Buschow, Vol. 9, Pages 57-302 Elsevier, Amsterdam, 1995.
- <sup>11</sup>V.P. Smilga and Yu.M. Belousov, *The Muon Method in Science*. Nova Science Publisher 1994.
- <sup>12</sup>E. Karlsson, *Solid State Phenomena, As Seen by Muons, Protons, and Excited Nuclei*. Clarendon, Oxford, 1995.
- <sup>13</sup>S.L. Lee, S.H. Kilcoyne, and R. Cywinski (eds.), *Muon Science: Muons in Physics; Chemistry and Materials*. IOP Publishing, Bristol and Philadelphia, 1999.
- <sup>14</sup>A. Yaouanc and P. D. de Réotier, *Muon Spin Rotation, Relaxation, and Resonance*, Oxford Science Publications, 2011.
- <sup>15</sup>S. J. Blundell, R. De Renzi, T. Lancaster, and F. L. Pratt (eds.) *Muon spectroscopy. An introduction*. Oxford: Oxford University Press, 2022.
- <sup>16</sup>S.J. Blundell, *Spin-Polarized Muons in Condensed Matter Physics*. *Contemporary Physics* **40**, 175-192 (1999).  
doi: 10.1080/001075199181521
- <sup>17</sup>P. Bakule and E. Morenzoni, *Generation and Application of Slow Polarized Muons*. *Contemporary Physics* **45**, 203 (2004).  
doi: 10.1080/00107510410001676803
- <sup>18</sup>A. Amato, *Heavy-fermion systems studied by  $\mu$ SR technique*. *Rev. Mod. Phys.* **69**, 1119 (1997).  
doi: 10.1103/RevModPhys.69.1119
- <sup>19</sup>P. Dalmas de Réotier and A. Yaouanc, *Muon Spin Rotation and relaxation in Magnetic Materials*. *J. Phys.: Condens. Matter* **9**, 9113 (1997).  
doi: 10.1088/0953-8984/9/43/002
- <sup>20</sup>J. Sonier, J. Brewer, and R. Kiefl,  *$\mu$ SR Studies of Vortex State in Type-II Superconductors*. *Rev. Mod. Physics* **72**, 769 (2000).  
doi: 10.1103/RevModPhys.72.769
- <sup>21</sup>R. Khasanov and Z. Guguchia, *Probing the multi gap behavior within '11' and '122' families of iron based superconductors: the muon-spin rotation studies*. *Superconductor Science and Technology* **28** 034003 (2015).  
doi: 10.1088/0953-2048/28/3/034003
- <sup>22</sup>J. F. Ziegler, J. P. Biersack, and M. D. Ziegler, *SRIM the stopping and range of ions in mater*. <http://www.srim.org>.
- <sup>23</sup>S. Klotz, *Techniques in high pressure neutron scattering*. Boca Raton, FL : CRC Press, 2013.
- <sup>24</sup>I.R. Walker, *Nonmagnetic piston-cylinder pressure cell for use at 35 kbar and above*. *Rev. Sci. Instrum.* **70**, 3402 (1999).  
doi: 10.1063/1.1149927
- <sup>25</sup>Y. Uwatoko, S. Todo, K. Ueda, A. Uchida, M. Kosaka, N. Mori, and T. Matsumoto, *Material properties of Ni-Cr-Al alloy and design of a 4 GPa class non-magnetic high-pressure cell*. *J. Phys.: Condens. Matter* **14**, 11291 (2002).  
doi: 10.1088/0953-8984/14/44/469
- <sup>26</sup>T. Goko, private communication.
- <sup>27</sup>[https://en.wikipedia.org/wiki/Quadrupole\\_magnet](https://en.wikipedia.org/wiki/Quadrupole_magnet)
- <sup>28</sup>A. Amato, H. Luetkens, K. Sedlak, A. Stoykov, R. Scheuermann, M. Elender, A. Raselli, and D. Graf, *The new versatile general purpose surface-muon instrument (GPS) based on silicon photomultipliers for  $\mu$ SR measurements on a continuous-wave beam*. *Rev. Sci. Instrum.* **88**, 093301 (2017).  
doi: 10.1063/1.4986045
- <sup>29</sup>Z. Salman, T. Prokscha, P. Keller, E. Morenzoni, H. Saadaoui, K. Sedlak, T. Shiroka, S. Sidorov, A. Suter, V. Vrankovic, and H.-P. Weber, *Design and Simulation of a Spin Rotator for Longitudinal Field Measurements in the Low Energy Muons Spectrometer*. *Phys. Procedia* **30**, 55 (2012).

- doi: 10.1016/j.phpro.2012.04.039
- <sup>30</sup>A. Stoykov, R. Scheuermann, K. Sedlak, T. Shiroka and V. Zhuk, *A new detector system for the ALC spectrometer—First experience with G-APDs in  $\mu$ SR instrumentation*. Physica B **404**, 986 (2009). doi: 10.1016/j.physb.2008.11.211
- <sup>31</sup>K. Sedlak, T. Shiroka, A. Stoykov and R. Scheuermann, *GEANT4 simulation of the upgraded ALC spectrometer*. Physica B **404**, 974 (2009). doi: 10.1016/j.physb.2008.11.214
- <sup>32</sup>K. Sedlak, R. Scheuermann, A. Stoykov and A. Amato, *GEANT4 simulation and optimisation of the high-field  $\mu$ SR spectrometer*. Physica B **404**, 970 (2009). doi: 10.1016/j.physb.2008.11.215
- <sup>33</sup>A. Stoykov, R. Scheuermann, K. Sedlak, J. Rodriguez, U. Greuter and A. Amato, *The 10 Tesla  $\mu$ SR instrument: detector solutions*. Phys. Procedia **30**, 7 (2012). doi: 10.1016/j.phpro.2012.04.028
- <sup>34</sup><https://www.psi.ch/en/low-energy-muons/experimental-setup>
- <sup>35</sup>K. Sedlak, R. Scheuermann, T. Shiroka, A. Stoykov, A. R. Raselli, and A. Amato, *MusrSim and MusrSimAna – simulation tools for  $\mu$ SR instruments*. Phys. Procedia **30**, 61 (2012). doi: 10.1016/j.phpro.2012.04.040
- <sup>36</sup>K. Sedlak, T. Shiroka, A. Stoykov, and R. Scheuermann, *Geant4 simulation of the new ALC  $\mu$ SR spectrometer*. IEEE Trans. Nucl. Sci. **57**, 2187 (2010). doi: 10.1109/TNS.2010.2052066
- <sup>37</sup>S. Agostinelli, et al., *Geant4 – a simulation toolkit*. Nucl. Inst. and Meth. in Phys. Res. A **506**, 250 (2003). doi: 10.1016/S0168-9002(03)01368-8250–303
- <sup>38</sup>J. Allison, et al., *Geant4 developments and applications*. IEEE Trans. Nucl. Sci. **53**, 270 (2006). doi: 10.1109/TNS.2006.869826
- <sup>39</sup>R. Brun and F. Rademakers, *ROOT – an object oriented data analysis framework*. Nucl. Inst. and Meth. in Phys. Res. A **389**, 81 (1997). doi: 10.1016/S0168-9002(97)00048-X
- <sup>40</sup><https://advansid.com>
- <sup>41</sup>P.W. Cattaneo, M. De Gerone, F. Gatti, M. Nishimura, W. Ootani, M. Rossella and Y. Uchiyama, *Development of High Precision Timing Counter Based on Plastic Scintillator with SiPM Readout*. IEEE Trans. Nucl. Sci. **61**, 2657 (2014). doi: 10.1109/TNS.2014.2347576
- <sup>42</sup>T. Prokscha, R. Scheuermann, U. Hartmann, A. Raselli, A. Suter, A. Amato, G.J. Nieuwenhuys, A. Dijksmann, F. Gartner, U. Greuter, S. Mutter, N. Schlumpf, and E. Morenzoni, *A novel VME based  $\mu$ SR data acquisition system at PSI*. Physica B **404**, 1007 (2009). doi: 10.1016/j.physb.2008.11.206
- <sup>43</sup>V. Grinenko, D. Das, R. Gupta, B. Zinkl, N. Kikugawa, Y. Maeno, C. W. Hicks, H.-H. Klauss, M. Sigrist and R. Khasanov, *Unsplit superconducting and time reversal symmetry breaking transitions in  $Sr_2RuO_4$  under hydrostatic pressure and disorder*. Nat. Commun. **12**, 3920 (2021). doi: 10.1038/s41467-021-24176-8
- <sup>44</sup>Z. Shermadini, *Iron based pnictide and chalcogenide superconductors studied by muon spin spectroscopy*. PhD thesis, Technical University Dresden, Germany, 2014.
- <sup>45</sup>M.I. Eremets, *High Pressure Experimental Methods*. Oxford University Press, 1996.
- <sup>46</sup>Rustem Khasanov, Gediminas Simutis, Yurii G. Pashkevich, Tatyana Shevtsova, William R. Meier, Mingyu Xu, Sergey L. Bud'ko, Vladimir G. Kogan, and Paul C. Canfield, *Magnetism and its coexistence with superconductivity in  $CaK(Fe_{0.949}Ni_{0.051})_4As_4$ : Muon spin rotation/relaxation studies*. Phys. Rev. B **102**, 094504 (2020). doi: 10.1103/PhysRevB.102.094504
- <sup>47</sup>R. Khasanov, Z. Guguchia, I. Eremin, H. Luetkens, A. Amato, P.K. Biswas, C. Rüegg, M.A. Susner, S.S. Athena S, N.D. Zhigadlo, and E. Morenzoni, *Pressure-induced electronic phase separation of magnetism and superconductivity in CrAs*. Scientific Reports **5**, 13788 (2015). doi: 10.1038/srep13788
- <sup>48</sup>R. Khasanov, A. Amato, P. Bonfá, Z. Guguchia, H. Luetkens, E. Morenzoni, R. De Renzi, and N. D. Zhigadlo, *High-pressure magnetic state of MnP probed by means of muon-spin rotation*. Phys. Rev. B **93**, 180509(R) (2016). doi: 10.1103/PhysRevB.93.180509
- <sup>49</sup>R. Khasanov, A. Amato, P. Bonfá, Z. Guguchia, H. Luetkens, E. Morenzoni, R. De Renzi, and N. D. Zhigadlo, *Magnetic states of MnP: muon-spin rotation studies*. J. Phys.: Condens. Matter **29**, 164003 (2017). doi:10.1088/1361-648X/aa6391
- <sup>50</sup>Rustem Khasanov, Zurab Guguchia, Elvezio Morenzoni, Chris Baines, Aifeng Wang, Xianhui Chen, Zbigniew Bukowski, and Fazel Tafti, *Pressure-induced magnetism in the iron-based superconductors  $AFe_2As_2$  ( $A=K, Cs, Rb$ )*. Phys. Rev. B **102**, 140502(R) (2020). doi: 10.1103/PhysRevB.102.140502
- <sup>51</sup>Elena Gati, Sergey L. Bud'ko, Lin-Lin Wang, Adrian Valadkhani, Ritu Gupta, Brinda Kuthanazhi, Li Xiang, John M. Wilde, Aashish Sapkota, Zurab Guguchia, Rustem Khasanov, Roser Valentí, and Paul C. Canfield, *Pressure-induced ferromagnetism in the topological semimetal  $EuCd_2As_2$* . Phys. Rev. B **104**, 155124 (2021). doi: 10.1103/PhysRevB.104.155124
- <sup>52</sup>Elena Gati, John M. Wilde, Rustem Khasanov, Li Xiang, Sachith Disnayake, Ritu Gupta, Masaaki Matsuda, Feng Ye, Bianca Haberl, Ud-hara Kaluarachchi, Robert J. McQueeney, Andreas Kreyssig, Sergey L. Bud'ko, and Paul C. Canfield, *Formation of short-range magnetic order and avoided ferromagnetic quantum criticality in pressurized  $LaCrGe_3$* . Phys. Rev. B **103**, 075111 (2021). doi: 10.1103/PhysRevB.103.075111
- <sup>53</sup>Rustem Khasanov, Hubertus Luetkens, Elvezio Morenzoni, Gediminas Simutis, Stephan Schönecker, Andreas Östlin, Liviu Chioncel, and Alex Amato, *Superconductivity of Bi-III phase of elemental bismuth: Insights from muon-spin rotation and density functional theory*. Phys. Rev. B **98**, 140504(R) (2018). doi: 10.1103/PhysRevB.98.140504
- <sup>54</sup>Z. Guguchia, D. Gawryluk, M. Brzezinska, S.S. Tsirkin, R. Khasanov, E. Pomjakushina, F.O. von Rohr, J. Vezzhak, M.Z. Hasan, T. Neupert, H. Luetkens, and A. Amato, *Nodeless Superconductivity and its Evolution with Pressure in the Layered Dirac Semimetal  $2M-WS_2$* . npj Quantum Materials **4**, 50 (2019). doi: 10.1038/s41535-019-0189-5
- <sup>55</sup>F.O. von Rohr, J.-C. Orain, R. Khasanov, Z. Shermadini, A. Nikitin, J. Chang, A.R. Wieteska, A.N. Pasupathy, M.Z. Hasan, A. Amato, H. Luetkens, Y.J. Uemura, and Z. Guguchia, *Linear Scaling of the Superfluid Density with the Critical Temperature in the Layered Superconductor  $2H-NbSe_2$* . Science Advances **5**, eaav8465 (2019). doi: 10.1126/sciadv.aav8465
- <sup>56</sup>N. Barbero, S. Hohenstein, T. Shang, Z. Shermadini, F. Lochner, I. Eremin, C. Wang, G.-H. Cao, R. Khasanov, H.-R. Ott, J. Mesot, and T. Shiroka, *Pressure effects on the electronic properties of the undoped superconductor  $ThFeAsN$* . Phys. Rev. B **97**, 140506(R) (2018). doi: 10.1103/PhysRevB.97.140506
- <sup>57</sup>Ritu Gupta, Debarchan Das, Charles Mielke III, Ethan Ritz, Fabian Hotz, Qiangwei Yin, Zhijun Tu, Chunsheng Gong, Hechang Lei, Turan Birol, Rafael M. Fernandes, Zurab Guguchia, Hubertus Luetkens, and Rustem Khasanov, *Two types of charge order in the superconducting kagome material  $CsV_3Sb_5$* . arXiv:2203.05055. doi: 10.48550/arXiv.2203.11785
- <sup>58</sup>G. M. Luke, Y. Fudamoto, K. M. Kojima, M. I. Larkin, J. Merrin, B. Nachumi, Y. J. Uemura, Y. Maeno, Z. Q. Mao, Y. Mori, H. Nakamura, and M. Sigrist, *Time-Reversal Symmetry Breaking Superconductivity in  $Sr_2RuO_4$* . Nature **394**, 558-561 (1998). doi: 10.1038/29038
- <sup>59</sup>G.M. Luke, A. Keren, L. P. Le, W. D Wu, Y. J. Uemura, D. A. Bonn, L. Taillefer, and J. D. Garrett, *Muon spin relaxation in  $UPt_3$* . Phys. Rev. Lett. **71**, 1466 (1993). doi: 10.1103/PhysRevLett.71.1466
- <sup>60</sup>A. Maisuradze, W. Schnelle, R. Khasanov, R. Gumeniuk, M. Nicklas, H. Rosner, A. Leithe-Jasper, Yu. Grin, A. Amato, and P. Thalmeier, *Evidence for time-reversal symmetry breaking in superconducting  $PrPt_4Ge_{12}$* . Phys. Rev. B **82**, 024524 (2010). doi: 10.1103/PhysRevB.82.024524
- <sup>61</sup>T. Shang, M. Smidman, S. K. Ghosh, C. Baines, L. J. Chang, D. J. Gawryluk, J. A. T. Barker, R. P. Singh, D. McK. Paul, G. Balakrishnan, E. Pomjakushina, M. Shi, M. Medarde, A. D. Hillier, H. Q. Yuan, J. Quintanilla, J. Mesot, and T. Shiroka, *Time-Reversal Symmetry Breaking in Re-Based*

- Superconductors*. Phys. Rev. Lett. **121**, 257002 (2018).  
doi: 10.1103/PhysRevLett.121.257002
- <sup>62</sup>S. K. Ghosh, M. Smidman, T. Shang, J. F. Annett, A. D. Hillier, J. Quintanilla, and H. Yuan, *Recent Progress on Superconductors with Time-Reversal Symmetry Breaking*. J. Phys.: Condens. Matter **33**, 033001 (2021).  
doi: 10.1088/1361-648x/abaa06
- <sup>63</sup>V. Grinenko, S. Ghosh, R. Sarkar, J.-C. Orain, A. Nikitin, M. Elender, D. Das, Z. Guguchia, F. Brückner, M. E. Barber, J. Park, N. Kikugawa, D. A. Sokolov, J. S. Bobowski, T. Miyoshi, Y. Maeno, A. P. Mackenzie, H. Luetkens, C. W. Hicks, and H.-H. Klauss, *Split superconducting and time-reversal symmetry-breaking transitions in  $Sr_2RuO_4$  under stress*. Nat. Phys. **17**, 748 (2021).  
doi: 10.1038/s41567-021-01182-7
- <sup>64</sup>V. Grinenko, R. Sarkar, K. Kihou, C.H. Lee, I. Morozov, S. Aswartham, B. Büchner, P. Chekhonin, W. Skrotzki, K. Nenkov, R. Hühne, K. Nielsch, S. L. Drechsler, V. L. Vadimov, M. A. Silaev, P. A. Volkov, I. Eremin, H. Luetkens, and H.-H. Klauss, *Superconductivity with broken time-reversal symmetry inside a superconducting s-wave state*. Nat. Phys. **16**, 789 (2020).  
doi: 10.1038/s41567-020-0886-9
- <sup>65</sup>C. Mielke III, D. Das, J.-X. Yin, H. Liu, R. Gupta, Y.-X. Jiang, M. Medarde, X. Wu, H.C. Lei, J.J. Chang, P. Dai, Q. Si, H. Miao, R. Thomale, T. Neupert, Y. Shi, R. Khasanov, M.Z. Hasan, H. Luetkens, and Z. Guguchia, *Time-reversal symmetry-breaking charge order in a kagome superconductor*. Nature **602**, 245-250 (2022).  
doi: 10.1038/s41586-021-04327-z
- <sup>66</sup>Z. Guguchia, C. Mielke III, D. Das, R. Gupta, J.-X. Yin, H. Liu, Q. Yin, M.H. Christensen, Z. Tu, C. Gong, N. Shumiya, Ts. Gamsakhurdashvili, M. Elender, Pengcheng Dai, A. Amato, Y. Shi, H.C. Lei, R.M. Fernandes, M.Z. Hasan, H. Luetkens, and R. Khasanov, *Tunable nodal kagome superconductivity in charge ordered  $RbV_3Sb_5$* . arXiv:2202.07713 (2022).
- <sup>67</sup>Rustem Khasanov, Debarchan Das, Ritu Gupta, Charles Mielke, III, Matthias Elender, Qiangwei Yin, Zhijun Tu, Chunsheng Gong, Hechang Lei, Ethan T. Ritz, Rafael M. Fernandes, Turan Birol, Zurab Guguchia, and Hubertus Luetkens, *Time-reversal symmetry broken by charge order in  $CsV_3Sb_5$* . Phys. Rev. Research **4**, 023244 (2022).  
doi: 10.1103/PhysRevResearch.4.023244
- <sup>68</sup>L. Yu, C. Wang, Y. Zhang, M. Sander, S. Ni, Z. Lu, S. Ma, Z. Wang, Z. Zhao, H. Chen, K. Jiang, Y. Zhang, H. Yang, F. Zhou, X. Dong, S. L. Johnson, M. J. Graf, J. Hu, H.-J. Gao, and Z. Zhao, *Evidence of a hidden flux phase in the topological kagome metal  $CsV_3Sb_5$* . arXiv:2107.10714 (2021).
- <sup>69</sup>Zhaoyang Shan, Pabitra K. Biswas, Sudeep K. Ghosh, T. Tula, Adrian D. Hillier, Devashibhai Adroja, Stephen Cottrell, Guang-Han Cao, Yi Liu, Xiaofeng Xu, Yu Song, Huiqiu Yuan, and Michael Smidman, *Muon-spin relaxation study of the layered kagome superconductor  $CsV_3Sb_5$* . arXiv:2203.05770 (2022).
- <sup>70</sup>Z. Guguchia, J. Verezhak, D. Gawryluk, S.S. Tsirkin, J.-X. Yin, I. Belopolski, H. Zhou, G. Simutis, S.-S. Zhang, T.A. Cochran, G. Chang, E. Pomjakushina, L. Keller, Z. Skrzeczowska, Q. Wang, H.C. Lei, R. Khasanov, A. Amato, S. Jia, T. Neupert, H. Luetkens, and M.Z. Hasan, *Tunable Berry Curvature Through Magnetic Phase Competition in a Topological Kagome Magnet*. Nature Communications **11**, 559 (2020).  
doi: 10.1038/s41467-020-14325-w
- <sup>71</sup>Z. Guguchia, A.M. dos Santos, F.O. von Rohr, J.J. Molaison, S. Banerjee, D. Rhodes, J.-X. Yin, R. Khasanov, J. Hone, Y.J. Uemura, M.-Z. Hasan, H. Luetkens, E.S. Bozin, and A. Amato, *Pressure induced topological quantum phase transition in Weyl semimetal  $Td-MoTe_2$* . J. Phys. Soc. Jpn. **89**, 094707 (2020).  
doi: 10.7566/JPSJ.89.094707
- <sup>72</sup>Z. Guguchia, B. A. Frandsen, D. Santos-Cottin, S. C. Cheung, Z. Gong, Q. Sheng, K. Yamakawa, A. M. Hallas, M. N. Wilson, Y. Cai, J. Beare, R. Khasanov, R. De Renzi, G. M. Luke, S. Shamoto, A. Gauzzi, Y. Klein, and Y. J. Uemura, *Probing the quantum phase transition in Mott insulator  $BaCoS_2$  tuned by pressure and Ni substitution*. Phys. Rev. Materials **3**, 045001 (2019).  
doi: 10.1103/PhysRevMaterials.3.045001
- <sup>73</sup>Z. Guguchia, R. Khasanov, A. Shengelaya, E. Pomjakushina, S. J. L. Billinge, A. Amato, E. Morenzoni, and H. Keller, *Cooperative coupling of static magnetism and bulk superconductivity in the stripe phase of  $La_{2-x}Ba_xCuO_4$ : Pressure- and doping-dependent studies*. Phys. Rev. B **94**, 214511 (2016).  
doi: 10.1103/PhysRevB.94.214511
- <sup>74</sup>M. Hiraishi, K. M. Kojima, H. Okabe, S. Takeshita, A. Koda, R. Kadono, R. Khasanov, S. Iimura, S. Matsuishi, and H. Hosono, *Magnetism driven by strong electronic correlations in the heavily carrier-doped iron oxypnictide  $LaFeAsO_{0.49}H_{0.51}$* . Phys. Rev. B **101**, 174414 (2020).  
doi: 10.1103/PhysRevB.101.174414
- <sup>75</sup>Jun Sugiyama, Daniel Andreica, Ola Kenji Forslund, Elisabetta Nocerino, Nami Matsubara, Yasmine Sassa, Zurab Guguchia, Rustem Khasanov, Francis L. Pratt, Hiroyuki Nakamura, and Martin Månsson, *Magnetic phase boundary of  $BaVS_3$  clarified with high-pressure  $\mu^+$ SR*. Phys. Rev. B **101**, 174403 (2020).  
doi: 10.1103/PhysRevB.101.174403
- <sup>76</sup>G. Lamura, I. J. Onuorah, P. Bonfà, S. Sanna, Z. Shermadini, R. Khasanov, J.-C. Orain, C. Baines, F. Gastaldo, M. Giovannini, I. Čurlík, A. Dzubinska, G. Pristas, M. Reiffers, A. Martinelli, C. Ritter, B. Joseph, E. Bauer, R. De Renzi, and T. Shiroka, *Pressure-induced antiferromagnetic dome in the heavy-fermion  $Yb_2Pd_2In_{1-x}Sn_x$  system*. Phys. Rev. B **101**, 054410 (2020).  
doi: 10.1103/PhysRevB.101.054410
- <sup>77</sup>S. Hohenstein, F. Hummel, Z. Guguchia, S. Kamusella, N. Barbero, H. Ogino, Z. Shermadini, R. Khasanov, A. Amato, T. Shiroka, H.-H. Klauss, E. Morenzoni, D. Johrendt, and H. Luetkens, *Coupled Magnetic and Superconducting Transitions in  $Sr_2VO_3FeAs$  Under Pressure*. Phys. Rev. B **104**, 104507 (2021).  
doi: 10.1103/PhysRevB.104.104507
- <sup>78</sup>S. Hohenstein, J. Stahl, Z. Shermadini, G. Simutis, V. Grinenko, D. A. Chareev, R. Khasanov, J.-C. Orain, A. Amato, H.-H. Klauss, E. Morenzoni, D. Johrendt, and H. Luetkens, *Extended Magnetic Dome Induced by Low Pressures in Superconducting  $FeSe_{1-x}S_x$* . Phys. Rev. Lett. **123**, 147001 (2019).  
doi: 10.1103/PhysRevLett.123.147001
- <sup>79</sup>Liangliang Zheng, Benjamin A. Frandsen, Changwei Wu, Ming Yi, Shan Wu, Qingzhen Huang, Edith Bourret-Courchesne, G. Simutis, R. Khasanov, Dao-Xin Yao, Meng Wang, and Robert J. Birgeneau, *Gradual enhancement of stripe-type antiferromagnetism in the spin-ladder material  $BaFe_2S_3$  under pressure*. Phys. Rev. B **98**, 180402(R) (2018).  
doi: 10.1103/PhysRevB.98.180402
- <sup>80</sup>G. Simutis, N. Barbero, K. Rolfs, P. Leroy-Calatayud, K. Mehlatat, R. Khasanov, H. Luetkens, E. Pomjakushina, Y. Singh, H.-R. Ott, J. Mesot, A. Amato, and T. Shiroka, *Chemical and hydrostatic-pressure effects on the Kitaev honeycomb material  $Na_2IrO_3$* . Phys. Rev. B **98**, 104421 (2018).  
doi: 10.1103/PhysRevB.98.104421
- <sup>81</sup>Rustem Khasanov, Rafael M. Fernandes, Gediminas Simutis, Zurab Guguchia, Alex Amato, Hubertus Luetkens, Elvezio Morenzoni, Xiaoli Dong, Fang Zhou, and Zhongxian Zhao, *Magnetic tricritical point and nematicity in  $FeSe$  under pressure*. Phys. Rev. B **97**, 224510 (2018).  
doi: 10.1103/PhysRevB.97.224510
- <sup>82</sup>Rustem Khasanov, Zurab Guguchia, Alex Amato, Elvezio Morenzoni, Xiaoli Dong, Fang Zhou, and Zhongxian Zhao, *Pressure-induced magnetic order in  $FeSe$ : A muon spin rotation study*. Phys. Rev. B **95**, 180504(R) (2017).  
doi: 10.1103/PhysRevB.95.180504
- <sup>83</sup>M. Majumder, R. Gupta, H. Luetkens, R. Khasanov, O. Stockert, P. Gegenwart, and V. Fritsch, *Spin-liquid signatures in the quantum critical regime of pressurized  $CePdAl$* . Phys. Rev. B **105**, L180402 (2022).  
doi: 10.1103/PhysRevB.105.L180402
- <sup>84</sup>M. Majumder, R. S. Manna, G. Simutis, J. C. Orain, T. Dey, F. Freund, A. Jesche, R. Khasanov, P. K. Biswas, E. Bykova, N. Dubrovinskaia, L. S. Dubrovinsky, R. Yadav, L. Hozoi, S. Nishimoto, A. A. Tsirlin, and P. Gegenwart, *Breakdown of Magnetic Order in the Pressurized Kitaev Irodate  $\beta-Li_2IrO_3$* . Phys. Rev. Lett. **120**, 237202 (2018).  
doi: 10.1103/PhysRevLett.120.237202
- <sup>85</sup>Ola Kenji Forslund, Daniel Andreica, Yasmine Sassa, Hiroshi Nozaki, Izumi Umegaki, Elisabetta Nocerino, Viktor Jonsson, Oscar Tjernberg, Zurab Guguchia, Zurab Shermadini, Rustem Khasanov, Masahiko Isobe, Hidenori Takagi, Yutaka Ueda, Jun Sugiyama, and Martin Månsson, *Magnetic phase diagram of  $K_2Cr_8O_{16}$  clarified by high-pressure muon spin*

- spectroscopy. *Sci Rep* **9**, 1141 (2019).  
doi: 10.1038/s41598-018-37844-5
- <sup>86</sup>Z. Guguchia, C. Mielke III, D. Das, R. Gupta, J.-X. Yin, H. Liu, Q. Yin, M.H. Christensen, Z. Tu, C. Gong, N. Shumiya, Ts. Gamsakhurdashvili, M. Elender, Pengcheng Dai, A. Amato, Y. Shi, H.C. Lei, R.M. Fernandes, M.Z. Hasan, H. Luetkens, and R. Khasanov, *Tunable nodal kagome superconductivity in charge ordered RbV<sub>3</sub>Sb<sub>5</sub>*. *arXiv:2202.07713*.  
doi: 10.48550/arXiv.2202.07713
- <sup>87</sup>Ola Kenji Forslund, Daniel Andreica, Yasmine Sassa, Masaki Imai, Chishiro Michioka, Kazuyoshi Yoshimura, Zurab Guguchia, Zurab Sher-madini, Rustem Khasanov, Jun Sugiyama, and Martin Månsson, *Pressure driven magnetic order in Sr<sub>1-x</sub>Ca<sub>x</sub>Co<sub>2</sub>P<sub>2</sub>*. *arXiv:2111.11962*.  
doi: 10.48550/arXiv.2111.11962
- <sup>88</sup>D. Das, R. Gupta, C. Baines, H. Luetkens, D. Kaczorowski, Z. Guguchia, and R. Khasanov, *Unconventional Pressure Dependence of the Superfluid Density in the Nodeless Topological Superconductor  $\alpha$ -PdBi<sub>2</sub>*. *Phys. Rev. Lett.* **127**, 217002 (2021).  
doi: 10.1103/PhysRevLett.127.217002
- <sup>89</sup>R. Khasanov, H. Luetkens, A. Amato, and E. Morenzoni, *Structural phases of elemental Ga: Universal relations in conventional superconductors*. *Phys. Rev. B* **101**, 054504 (2020).  
doi: 10.1103/PhysRevB.101.054504
- <sup>90</sup>R. Khasanov, M.M. Radonjić, H. Luetkens, E. Morenzoni, G. Simutis, S. Schönecker, and W.H. Appelt, A. Östlin, L. Chioncel, and A. Amato, *Superconducting nature of the Bi-II phase of elemental bismuth*. *Phys. Rev. B* **99**, 174506 (2019).  
doi: doi.org/10.1103/PhysRevB.99.174506
- <sup>91</sup>Rustem Khasanov and Igor I. Mazin, *Anomalous gap ratio in anisotropic superconductors: Aluminum under pressure*. *Phys. Rev. B* **103**, L060502 (2021).  
doi: 10.1103/PhysRevB.103.L060502
- <sup>92</sup>J.-G. Cheng, K. Matsubayashi, W. Wu, J. P. Sun, F. K. Lin, J. L. Luo, and Y. Uwatoko, *Pressure Induced Superconductivity on the border of Magnetic Order in MnP*. *Phys. Rev. Lett.* **114**, 117001 (2015).  
doi: 10.1103/PhysRevLett.114.117001
- <sup>93</sup>Y. Maeno, H. Hashimoto, K. Yoshida, S. Nishizaki, T. Fujita, J. Bednorz, and F. Lichtenberg, *Superconductivity in a layered perovskite without copper*. *Nature* **372**, 532 (1994).  
doi: 10.1038/372532a0
- <sup>94</sup>A. P. Mackenzie, and Y. Maeno, *The superconductivity of Sr<sub>2</sub>RuO<sub>4</sub> and the physics of spin-triplet pairing*. *Rev. Mod. Phys.* **75**, 657 (2003).  
doi: 10.1103/RevModPhys.75.657
- <sup>95</sup>A. P. Mackenzie, T. Scaffidi, C. W. Hicks, and Y. Maeno, *Even odder after twenty-three years: the superconducting order parameter puzzle of Sr<sub>2</sub>RuO<sub>4</sub>*. *npj Quantum Materials* **2**, 40 (2017).  
doi: 10.1038/s41535-017-0045-4
- <sup>96</sup>Y. Maeno, S. Kittaka, T. Nomura, S. Yonezawa, and K. Ishida, *Evaluation of Spin-Triplet Superconductivity in Sr<sub>2</sub>RuO<sub>4</sub>*. *J. Phys. Soc. Jpn.* **81**, 011009 (2012).  
doi: 10.1143/JPSJ.81.011009
- <sup>97</sup>C. Kallin, *Chiral p-wave order in Sr<sub>2</sub>RuO<sub>4</sub>*. *Rep. Prog. Phys.* **75**, 042501 (2012).  
doi: 10.1088/0034-4885/75/4/042501
- <sup>98</sup>Jing Xia, Yoshiteru Maeno, Peter T. Beyersdorf, M. M. Fejer, and Aharon Kapitulnik, *High Resolution Polar Kerr Effect Measurements of Sr<sub>2</sub>RuO<sub>4</sub>: Evidence for Broken Time-Reversal Symmetry in the Superconducting State*. *Phys. Rev. Lett.* **97**, 167002 (2006).  
doi: 10.1103/PhysRevLett.97.167002
- <sup>99</sup>K. Ishida, H. Mukuda, Y. Kitaoka, K. Asayama, Z. Q. Mao, Y. Mori, and Y. Maeno, *Spin-triplet superconductivity in Sr<sub>2</sub>RuO<sub>4</sub> identified by <sup>17</sup>O Knight shift*. *Nature* **396**, 658 (1998).  
doi: 10.1038/25315
- <sup>100</sup>T. Nakamura, T. Sumi, S. Yonezawa, T. Terashima, M. Sigrist, H. Kaneyasu, and Y. Maeno, *Essential Configuration of Pb/Ru/Sr<sub>2</sub>RuO<sub>4</sub> Junctions Exhibiting Anomalous Superconducting Interference*. *J. Phys. Soc. Jpn.* **81**, 064708 (2012).  
doi: 10.1143/JPSJ.81.064708
- <sup>101</sup>M. S. Anwar, T. Nakamura, S. Yonezawa, M. Yakabe, R. Ishiguro, H. Takayanagi and Y. Maeno, *Anomalous switching in Nb/Ru/Sr<sub>2</sub>RuO<sub>4</sub> topological junctions by chiral domain wall motion*. *Sci. Rep.* **3**, 2480 (2013).  
doi: 10.1038/srep02480
- <sup>102</sup>A. Steppke, L. Zhao, M. E. Barber, T. Scaffidi, F. Jerzembeck, H. Rosner, A. S. Gibbs, Y. Maeno, S. H. Simon, A. P. Mackenzie, and C. W. Hicks, *Strong peak in T<sub>c</sub> of Sr<sub>2</sub>RuO<sub>4</sub> under uniaxial pressure*. *Science* **355**, eaaf9398 (2017).  
doi: 10.1126/science.aaf9398
- <sup>103</sup>A. Pustogow, Yongkang Luo, A. Chronister, Y.-S. Su, D. A. Sokolov, F. Jerzembeck, A. P. Mackenzie, C. W. Hicks, N. Kikugawa, S. Raghu, E. D. Bauer, and S. E. Brown, *Constraints on the superconducting order parameter in Sr<sub>2</sub>RuO<sub>4</sub> from oxygen-17 nuclear magnetic resonance*. *Nature* **574**, 72 (2019).  
doi: 10.1038/s41586-019-1596-2
- <sup>104</sup>K. Ishida, M. Manago, and Y. Maeno, *Reduction of the 17O Knight Shift in the Superconducting State and the Heat-up Effect by NMR Pulses on Sr<sub>2</sub>RuO<sub>4</sub>*. *J. Phys. Soc. Jpn.* **89**, 034712 (2020).  
doi: 10.7566/JPSJ.89.034712
- <sup>105</sup>J.W. Rohlf, *Modern Physics from  $\alpha$  to Z<sup>0</sup>*. Wiley-VCH, New-York, 1994.
- <sup>106</sup>C. Kittel, *Introduction to Solid State Physics, 7th Ed.*, Wiley, India, Pvt. Limited, 2007.
- <sup>107</sup>C. Poole, H. Farach, R. Creswick, and R. Prozorov, *Superconductivity 3rd Edition*, Elsevier: Amsterdam, 2014.
- <sup>108</sup>H. Leng, C. Paulsen, Y.K. Huang, and A. de Visser, *Type-I superconductivity in the Dirac semimetal PdTe<sub>2</sub>*. *Phys. Rev. B* **96**, 220506(R) (2017).  
doi: 10.1103/PhysRevB.96.220506
- <sup>109</sup>O. Prakash, A. Kumar, A. Thamizhavel, and S. Ramakrishnan, *Evidence for bulk superconductivity in pure bismuth single crystals at ambient pressure*. *Science* **355**, 52 (2017).  
doi: 10.1126/science.aaf8227
- <sup>110</sup>D. Campanini, Z. Diao, and A. Rydh, *Raising the superconducting T<sub>c</sub> of gallium: In situ characterization of the transformation of  $\alpha$ -Ga into  $\beta$ -Ga*. *Phys. Rev. B* **97**, 184517 (2018).  
doi: doi.org/10.1103/PhysRevB.97.184517
- <sup>111</sup>J. Beare, M. Nugent, M.N. Wilson, Y. Cai, T.J.S. Munsie, A. Amon, A. Leithe-Jasper, Z. Gong, S.L. Guo, Z. Guguchia, Y. Grin, Y.J. Uemura, E. Svanidze, and G.M. Luke,  *$\mu$ SR and magnetometry study of the type-I superconductor BeAu*. *Phys. Rev. B* **99**, 134510 (2019).  
doi: doi.org/10.1103/PhysRevB.99.134510
- <sup>112</sup>R. Karl, F. Burri, A. Amato, M. Donegà, S. Gvasaliya, H. Luetkens, E. Morenzoni, and R. Khasanov, *Muon spin rotation study of type-I superconductivity: Elemental  $\beta$ -Sn*. *Phys. Rev. B* **99**, 184515 (2019).  
doi: 10.1103/PhysRevB.99.184515
- <sup>113</sup>Rustem Khasanov, Ritu Gupta, Debarchan Das, Alfred Amon, Andreas Leithe-Jasper, and Eteri Svanidze, *Multiple-gap response of type-I non-centrosymmetric BeAu superconductor*. *Phys. Rev. Research* **2**, 023142 (2020).  
doi: 10.1103/PhysRevResearch.2.023142
- <sup>114</sup>Rustem Khasanov, Ritu Gupta, Debarchan Das, Andreas Leithe-Jasper, and Eteri Svanidze, *Single-gap versus two-gap scenario: Specific heat and thermodynamic critical field of the noncentrosymmetric superconductor BeAu*. *Phys. Rev. B* **102**, 014514 (2020).  
doi: 10.1103/PhysRevB.102.014514
- <sup>115</sup>Rustem Khasanov, Debarchan Das, Dariusz Jakub Gawryluk, Ritu Gupta, and Charles Mielke III, *Isotropic single-gap superconductivity of elemental Pb*. *Phys. Rev. B* **104**, L100508 (2021).  
doi: 10.1103/PhysRevB.104.L100508